UNIVERSITY OF BIRMINGHAM
University of Birmingham Research at Birmingham

Low-cost, high-resolution, drone-borne SAR imaging

Bekar, Ali; Antoniou, Michail; Baker, Chris

DOI:
10.1109/TGRS.2021.3085235

License:
Other (please specify with Rights Statement)

Document Version
Peer reviewed version

Citation for published version (Harvard):
Bekar, A, Antoniou, M & Baker, C 2021, 'Low-cost, high-resolution, drone-borne SAR imaging', *IEEE Transactions on Geoscience and Remote Sensing*, vol. 60, 5208811.
https://doi.org/10.1109/TGRS.2021.3085235

Link to publication on Research at Birmingham portal

Publisher Rights Statement:
© 2021 IEEE. Personal use of this material is permitted. Permission from IEEE must be obtained for all other uses, in any current or future media, including reprinting/republishing this material for advertising or promotional purposes, creating new collective works, for resale or redistribution to servers or lists, or reuse of any copyrighted component of this work in other works.

A. Bekar, M. Antoniou and C. J. Baker, "Low-Cost, High-Resolution, Drone-Borne SAR Imaging," in IEEE Transactions on Geoscience and Remote Sensing, doi: 10.1109/TGRS.2021.3085235.

General rights
Unless a licence is specified above, all rights (including copyright and moral rights) in this document are retained by the authors and/or the copyright holders. The express permission of the copyright holder must be obtained for any use of this material other than for purposes permitted by law.

•Users may freely distribute the URL that is used to identify this publication.
•Users may download and/or print one copy of the publication from the University of Birmingham research portal for the purpose of private study or non-commercial research.
•User may use extracts from the document in line with the concept of 'fair dealing' under the Copyright, Designs and Patents Act 1988 (?)
•Users may not further distribute the material nor use it for the purposes of commercial gain.

Where a licence is displayed above, please note the terms and conditions of the licence govern your use of this document.

When citing, please reference the published version.

Take down policy
While the University of Birmingham exercises care and attention in making items available there are rare occasions when an item has been uploaded in error or has been deemed to be commercially or otherwise sensitive.

If you believe that this is the case for this document, please contact UBIRA@lists.bham.ac.uk providing details and we will remove access to the work immediately and investigate.

Download date: 14. May. 2024

Low-cost, High-resolution, Drone-borne SAR Imaging

Ali Bekar, Michail Antoniou, Christopher J. Baker

***Abstract*— This paper develops and examines methods for the production of real-world, very high-resolution imagery using a high-frequency drone-borne synthetic aperture radar (SAR) operating at short-ranges. The significance of motion errors which lead to space-invariant/variant phase errors is discussed. Subsequently, an imaging algorithm capable of handling these errors is proposed and presented. The validity of the approach is tested through both simulation and experiment. We present novel short-range, fine-resolution imagery (less than 2 cm in cross-range) of an extended target area generated using a low-cost drone borne vehicular frequency-modulated continuous-wave (FMCW) radar operating at 77 GHz, without employing a dedicated inertial navigation system (INS) or global positioning system (GPS).**

***Index Terms*—Drone SAR, mini-UAV SAR, high-resolution imagery.**

I. Introduction

SYNTHETIC Aperture Radar (SAR) has been extensively developed and, subsequently, widely used as a remote sensing tool [1], [2]. Previous research has, almost exclusively, used airborne and spaceborne platforms to carry the radar sensor. As a new platform, drones have a number of unique characteristics, which are already opening up new applications for SAR imaging. Drones are cheap, easily accessible and rapidly deployable. Drones can follow trajectories and fly into areas which are otherwise difficult for conventional air or space-craft, if possible at all. However, they can only carry compact light-weight payloads and the prime power available to a radar sensor is severely restricted. This means that drone borne SAR imaging is more suitable for operating at relatively short ranges, in many instances, consistent with difficult to access areas of air-space. Further, drones are more prone to flight irregularities due to wind and turbulence, which, combined with inaccuracies of modern on-board inertial navigation system (INS) or global positioning system (GPS), potentially, makes image formation more challenging. Typically, the accuracy of a GPS on a drone is between 0.5 m and 2 m. This can be increased to centimetre level by using real-time-kinematic (RTK) or differential systems. However, this would begin to make the SAR system expensive.

There are systems that can rely on capable positional instrumentation, where the spatial variance of errors is low in both range and azimuth. For example, in [3] – [6], drone-borne SAR systems using ground penetrating radar (GPR) were introduced with the aim of underground imaging for landmine detection. Undesired motion errors were compensated by using GPS-RTK systems. In these reports, due to the low operating frequencies, the GPS-RTK system provides sufficiently accurate positional data to compensate for motion errors. Some systems use dedicated GPS/INS to ease the implementation of the autofocus algorithms. As an example, in [7], a high-resolution SAR image was generated using a Ku-band radar. A differential-GPS was employed to give high accuracy positional data. After, motion compensation (MoCo) with GPS data, the phase gradient algorithm (PGA) and minimum entropy algorithm (MEA) are implemented to compensate residual phase errors. Back-projection (BP) was used as an imaging algorithm. The reported W-band mini-SAR system in [8] uses a motion compensation method based on fusing a combination of the inertial measurement unit (IMU) and SAR data. In experimentation, the maximum imaging range was set at 600 m. Imagery with 4.5 cm range and 3.5 cm cross-range resolution was produced. Systems that do not rely on dedicated positioning systems have also been reported. For example, in [9], horizontal, vertical, and circular trajectories and repeat-pass interferometry using a drone-based system were investigated. The experiments were carried out using a 10 GHz radar. Phase errors were compensated using the phase history of point-like scatterers and polarimetric active radar calibrators. The resolution achieved was approximately 30 cm. However, space-variant phase errors were not apparent. In [10], a method was proposed to deal with range-azimuth coupling using a squint minimization technique. Squinted Azimuth-dependent PGA and MEA were used as autofocus algorithms. As a result, imagery with a resolution of 20 cm in cross-range was obtained using a 35 GHz radar. Employing the same SAR system as [7], [11] made the phase errors spatially invariant and formed imagery without using navigational data. A Quasi-Polar-Based fast factorized back-projection (FFBP) algorithm was proposed that also terminates the dependency on navigational data. Although FFBP is computationally less expensive than BP, it is not as fast as frequency domain algorithms. Approximately, a 4 cm cross-range resolution was achieved. In [12] and [13], a drone-borne SAR system was reported using a 9.7 GHz radar. A 10 cm resolution was reported using a 2D autofocus method after application of a polar format algorithm (PFA). In the experiment, the slant range to the scene center was around 2.5

The authors are with the School of Electronic, Electrical and Systems Engineering, University of Birmingham, Birmingham B15 2TT, U.K. (e-mail: m.antoniou@bham.ac.uk).

The work of Ali Bekar was supported by the Ministry of National Education, Republic of Turkey.

km. In the case of finer resolutions at high-frequencies and shorter ranges, high degrees of spatial variance will exist, and methods will be needed to correct them without the use of a dedicated INS.

The objective of the research presented here, is to create an image formation algorithm that can push the spatial resolution limits for short-range, very high-resolution drone-borne SAR imaging without the use of an on-board dedicated INS. In the algorithm developed, some of the range walk and phase errors are compensated by the help of the positional information provided by the drone's flight controller. Subsequently, local quadratic map-drift (LQMD) [14], [15] and PGA techniques are applied, respectively, to correct for residual range walk error and to compensate space-invariant phase errors. After range cell migration correction (RCMC), the image is divided into range and azimuth blocks and the residual phase errors are estimated and compensated within each local scene using PGA. Next, by applying another LQMD to each range block, discontinuities between azimuth blocks are reduced. The final image is formed using a Range Doppler Algorithm (RDA). The validity of the approach is tested through simulation and experiment. The experimental demonstrator built for this purpose comprised a hexacopter drone equipped with a low-cost, 77 GHz frequency-modulated continuous-wave (FMCW) radar system (RadarBook from the INRAS Company) originally developed for advanced automotive applications. In this way, images with resolution that would otherwise require advanced, multi-million airborne SAR, can now be formed with drone-borne SAR that costs orders of magnitude less (approximately £15k).

The rest of this paper is organized as follows. Section II explains the imaging geometry and the sources of motion error. Section III explains the imaging algorithm with simulation result shown in Section IV. The experimental setup and results are presented in Section V. Finally, discussion and conclusions are included in Section VI.

II. Imaging Geometry and Motion Error

The imaging geometry is very similar to strip-map mode airborne SAR (Fig. 1). The differences arise due to the altitude, the platform velocity, and the motion characteristics of the platform. Drones have low altitude, low velocity, and generally, are less-stable platforms. Also, some of the assumptions made in airborne SAR such as narrow beam and constant target height may not be applicable for short-range operation.

Ideally, the platform moves on a straight line with a constant velocity v and altitude h during the aperture time u_a. On the other hand, the actual trajectory has deviations due to turbulence. In Fig. 1, P indicates the ideal position of the platform whereas $\tilde{P}$ shows its actual position. The instantaneous motion error consists of cross-range motion errors, $\Delta e_x(u)$, and down-range motion errors, $\Delta e_y(u)$ and $\Delta e_z(u)$, where u is slow-time and between $\mp\frac{u_a}{2}$. If the ideal sensor position is assumed as $(vu, 0, h)$, the ideal slant range, R_i, to the target located at the point, (x_t, y_t, z_t), can be written as

$$R_i(u) = \sqrt{(vu - x_t)^2 + {y_t}^2 + (h - z_t)^2} \qquad (1)$$

Also, the closest approach to the target can be described as

$$R_0 = \sqrt{{y_t}^2 + (h - z_t)^2} \qquad (2)$$

The actual slant range, $R(u)$, is given as

$$R(u) = \sqrt{(vu + \Delta e_x(u) - x_t)^2 + \left(\Delta e_y(u) - y_t\right)^2 + (h + \Delta e_z(u) - z_t)^2} \qquad (3)$$

The range error in the line-of-sight (LOS) direction, $R_{er}(u)$, is the difference between the actual and the ideal range histories $R(u) - R_i(u)$. If $y_t >> \Delta e_y$ and $h >> \Delta e_z$, after Taylor expansion, $R_{er}(u)$ can be written as

$$R_{er}(u) \cong \frac{(vu - x_t)}{R_i(u)}\Delta e_x(u) - \frac{y_t}{R_i(u)}\Delta e_y(u) + \frac{h - z_t}{R_i(u)}\Delta e_z(u) \qquad (4)$$

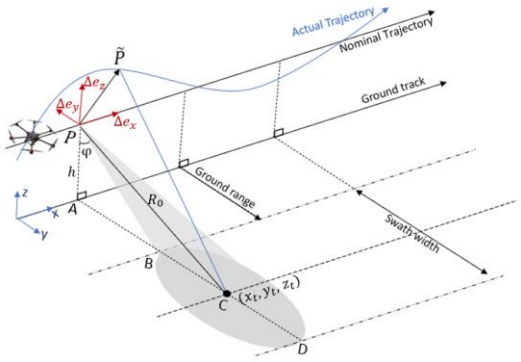

Fig. 1. Drone-borne SAR image geometry

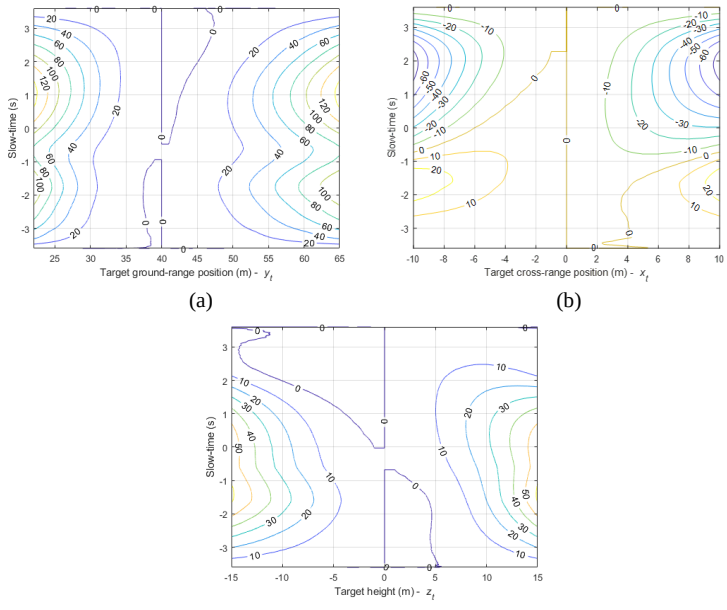

(a) (b) (c)

Fig. 2. (a) Residual phase error depending on ground range, y_t, for target position (0, y_t, 0), compensated based on target at (0, 40, 0). (b) Residual phase error depending on cross-range, x_t, for target position (x_t, 40, 0), compensated based on target at (0, 40, 0). (c) Residual phase error depending on height, z_t, for target position (0, 40, z_t), compensated based on target at (0, 40, 0). Phase errors are shown in radians.

To get a more realistic sense of motion errors and their dynamics, positional information extracted from the flight controller of our drone during flight was used. The trajectory itself is shown in the simulations in Section IV (Fig. 5 (a)). The

resulting phase error, $\frac{4\pi}{\lambda}R_{er}(u)$, was evaluated using (4), and the phase error difference to a reference target located at $(x_t, y_t, z_t) = (0, 40, 0)$ (without linear term) is presented in Fig. 2. The figure shows how the phase errors (in radians) depend on the target's position (x_t, y_t, z_t) at a frequency of 77 GHz. Here, h is assumed as 20 m whereas v is 5 m/s. In Fig. 2 (a), the phase error versus the target's ground range is plotted, assuming $(x_t, z_t) = (0, 0)$. The phase error is calculated for each slow-time position by changing the target's ground range. The linear term is removed, and the phase error is compensated based on the reference target. As expected, the error increases further away from the center and reaches up to 120 radians at the edge. In Fig. 2 (b), after subtracting the linear phase error and the error of the reference target, the phase error change depending on the target's cross-range position is demonstrated, assuming $(y_t, z_t) = (40, 0)$. The resulting error is changing between +20 and −60 radians. Finally, in Fig. 2 (c), by assuming $(x_t, y_t) = (0, 40)$, the phase error change is shown against the target's height after subtracting the linear phase error and the reference target's error. The resulting error can exceed 20 radians for a target which has 10 m height. As seen, the residual phase errors are high and changing non-linearly depending on the target position. Ultimately, this spatial variance limits the imaging capability even at short-ranges.

III. Imaging Algorithm

The flow-chart representing the algorithm is shown in Fig. 3. Fundamentally, after GPS/INS based MoCo, LQMD and PGA are implemented to compensate space-invariant errors. Then, based on azimuth and range blocking, space-variant errors are compensated locally. Although the accuracy of standard GPS/INS onboard drones is not as high as RTK measurements, it still has the potential to compensate at least some of the bulk motion errors. Nonetheless, significant phase and range-walk errors remain after GPS/INS based MoCo. Therefore, autofocus algorithms must also be employed. PGA is widely used to form high resolution SAR imagery. However, its performance is degraded if the amount of range-walk is high. Therefore, an option is to apply LQMD before PGA. LQMD can make accurate phase error estimations despite range-walk error. Also, it can estimate higher order phase errors compared to the conventional MD. After LQMD phase error estimation, range walk error is corrected, and the phase error is compensated. Nevertheless, LQMD is not a perfect algorithm to estimate higher-order motion errors. Also, these types of error can degrade image quality. In most cases, the data is not still accurate enough for RCMC due to residual errors. Consequently, PGA is applied to correct residual errors. At the short-ranges considered here, the footprint of the beam is small. This leads to less prominent targets within the beam. Also, target location may affect the phase error as shown in Fig. 2. As a result, it is not always possible to compensate space-variant errors globally. Therefore, a strategy is followed that is based on range/azimuth blocks. The residual phase errors within the local scenes are estimated by PGA and then compensated. Also, by implementing another LQMD to each range-block, discontinuities between the azimuth blocks are reduced. This method does not promise a global solution, and the image quality may vary from one local image to another. On the other hand, the method is easy to implement and has the potential to give satisfying results, as will be shown later.

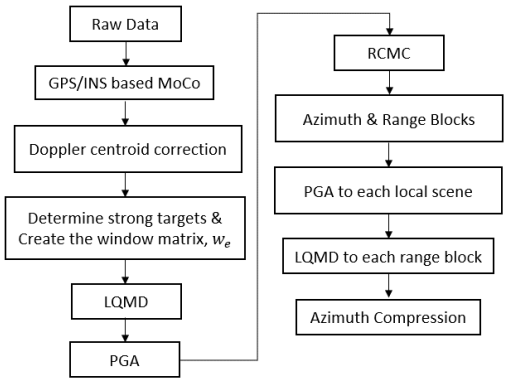

Fig. 3. The flow chart of the algorithm.

The received signal of an FMCW radar is given as

$$s(t,u) = A \cdot p(t - \frac{2R(u)}{c}) \cdot e^{j2\pi f_c\left(t-\frac{2R(u)}{c}\right)} \cdot e^{j\pi\gamma\left(t-\frac{2R(u)}{c}\right)^2} \quad (5)$$

where A includes the antenna's azimuth pattern, the second term is the envelope of the transmitted signal, $\frac{-T_m}{2} \leq t < \frac{T_m}{2}$, $\frac{-u_a}{2} \leq u < \frac{u_a}{2}$, T_m is the sweep time, f_c is the center frequency, c is the light speed and γ is the chirp rate.

After demodulation, the received signal can be represented by the below equation.

$$\tilde{s}(t,u) = s(t,u) \cdot h(t)^* = A \cdot p\left(t - \frac{2R(u)}{c}\right) \cdot p(t)^* \cdot e^{-j2\pi f_c \frac{2R(u)}{c}} \cdot e^{-j2\pi\left(\gamma\frac{2R(u)}{c}\right)t} \cdot e^{j\pi\gamma\left(\frac{2R(u)}{c}\right)^2} \quad (6)$$

where $h(t)$ is the transmitted signal and the symbol $[\cdot]^*$ denotes the complex conjugate.

As shown in Section II, $R(u)$ can be written as a summation of the ideal range history and the range error history. As a result, the signal which represents the two-dimensional error function, $s_e(t,u)$, can be written as

$$s_e(t,u) = \Phi_1(u) \cdot \Phi_2(t,u) \cdot \Phi_3(u) = e^{-j2\pi f_c \frac{2R_{er}(u)}{c}} \cdot e^{-j2\pi\left(\gamma\frac{2R_{er}(u)}{c}\right)t} \cdot e^{j\pi\gamma\left(\frac{4R_{er}(u)\left(2R_i(u)+R_{er}(u)\right)}{c^2}\right)} \quad (7)$$

Here, the second term is both a fast and slow-time dependent error whereas the first and third terms are only slow-time dependent. These three terms are represented by $\Phi_1(u)$, $\Phi_2(t,u)$, $\Phi_3(u)$, respectively. The contribution of $\Phi_3(u)$ is generally low enough to neglect it. The main phase error is caused by $\Phi_1(u)$, whereas $\Phi_2(t,u)$ results in range walk error in the image.

A. GPS/INS Based MoCo

In the first step, GPS/INS data is used for coarse MoCo. At first, most of the range walk error is corrected using $\Phi_2(t,u)$, referenced to the scene centre, by exploiting the shift theorem. Next, the phase error, $\Phi_1(u)$, is compensated on the range-

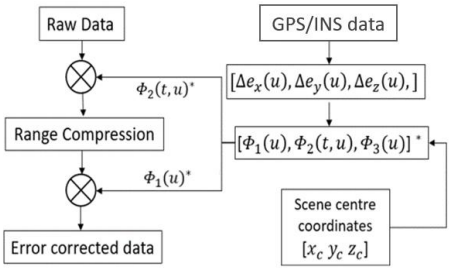

Fig. 4. GPS/INS based MoCo.

compressed data as shown in Fig. 4. The third term, $\Phi_3(u)$, is low and negligible because γ/c^2 is very small. Also, the Doppler centroid is estimated and then shifted to zero Doppler. It is worth noting that the phase error function generated using the GPS/INS data cannot be used to compensate the range dependent errors as in the two-step MoCo [16] due to the low accuracy of GPS/INS. At the end of this stage, although less than $s_e(t,u)$, the error function, $\tilde{s}_e(t,u)$, still includes both phase error and range walk error. The range compressed signal after GPS/INS based MoCo can be written as

$$\tilde{s}(f_r,u) = \int_{-\frac{T_m}{2}}^{\frac{T_m}{2}} \tilde{s}_i(t,u)\cdot \tilde{s}_e(t,u)\cdot e^{-j2\pi f_r t}dt \qquad (8)$$

where $\tilde{s}_i(f_r,u)$ represents the ideal range compressed signal and f_r represents range frequency. The slant range, r, can be expressed as $cf_r/2\gamma$.

B. Space-Invariant Phase Error Estimation

In the second step, the residual space-invariant phase error is estimated in a similar way with LQMD [14]. However, before autofocusing, more suitable parts of the data must be determined for the error estimation process. This is because the antenna footprint is small, and there are limited prominent targets within the beam. Firstly, the positions of prominent/strong targets are determined in the coarse image generated after GPS/INS based MoCo. The range history of each target is limited by the target's location and the beamwidth of the antenna. The length of the target's range history in azimuth, L_t, is described as

$$L_t = 2R_0 tan(\theta/2) \qquad (9)$$

where θ is beamwidth of the antenna.

When targets are selected from a particular range, at least N_t targets, uniformly distributed along azimuth direction must exist. However, in most cases, strong targets are randomly distributed. To enhance the phase error estimation, targets' range histories are windowed, and other parts of the data are set to 0. This is achieved by multiplying the data, $\tilde{s}(f_r,u)$, by the window matrix, w_e, which has the same size as $\tilde{s}(f_r,u)$ and consist of ones and zeros depending on the targets' positions and L_t. However, there must be at least one range sample which is different from zero for each azimuth sample.

$$N_t = \frac{vu_a}{L_t} \qquad (10)$$

Subsequently, the data is divided into half overlapped, N_b, azimuth blocks.

$$N_b = \frac{2u_a}{u_{s_l}} - 1 \qquad (11)$$

where u_{s_l} is the azimuth block time for LQMD.

Then, each block is de-chirped (12) and divided into two parts. After converting the data into frequency domain, two local intensity images are generated as in (13) and (14).

$$s_{ab}(f_r,u) = w_e\cdot \tilde{s}(f_r,u)\cdot e^{j\pi\frac{2v^2\left(u-\frac{(nu_{s_l}-u_a)}{2}\right)^2}{\lambda r}} \qquad (12)$$

where $\frac{(n-1)u_{s_l}-u_a}{2} \le u < \frac{(n+1)u_{s_l}-u_a}{2}$, s_{ab} is the de-chirped signal for each azimuth block and n is nth (n = $1,2,\cdots,N_b$) azimuth block.

$$S_L(f_r,f_a) = \left|\int_{\frac{-u_{s_l}}{2}}^{0} s_{ab}(f_r,u)\cdot e^{-j2\pi f_a u}du\right|^2 \qquad (13)$$

$$S_R(f_r,f_a) = \left|\int_{0}^{\frac{u_{s_l}}{2}} s_{ab}(f_r,u)\cdot e^{-j2\pi f_a u}\,du\right|^2 \qquad (14)$$

where f_a is the azimuth frequency, $S_L(f_r,f_a)$ and $S_R(f_r,f_a)$ represent the left and right part intensity image of each azimuth block, respectively.

In the presence of phase errors, the peak position of the cross-correlation of the two images is shifted. Cross-correlation functions of each range-bin are incoherently summed for a more accurate estimation as

$$c_n(\Delta f) = \sum_{r_b=1}^{N_r}\int S_L(r_b,f_a)\cdot S_R(r_b,f_a+\Delta f)df_a \qquad (15)$$

where $\frac{-f_{PRF}}{2} \le \Delta f < \frac{f_{PRF}}{2}$, f_{PRF} is pulse repetition frequency, $c_n(\Delta f)$ is the cross-correlation response of the nth azimuth block, r_b indicates a particular range-bin and N_r is the number of range-bins.

The local quadratic phase error coefficient is given as $2\pi\frac{\Delta f_m}{u_{s_l}}$ where Δf_m is the relative shift extracted from $c_n(\Delta f)$. Local quadratic phase error coefficients for each azimuth block are stored in a vector as $\frac{2\pi}{u_{s_l}}[\Delta f_{m_1}, \Delta f_{m_2}, \cdots, \Delta f_{m_{N_b}}]$. After interpolating this vector, the second derivative of the phase error function, $\emptyset''(u)$, is obtained as explained in [14] and [15]. Next, double integration is applied to this function to produce the final phase error function, $\emptyset_{MD}(u)$.

$$\emptyset_{MD}(u) = \iint_{-u_a/2}^{u_a/2} \emptyset''(u)\,dudu \qquad (16)$$

As shown in (17), the estimated phase error is used first to correct range walk error in the range-time domain, then to compensate the phase error in the range-frequency domain. The correction functions are formed using $\Phi_1(u)$ and $\Phi_2(t,u)$ in (7).

$$\tilde{s}_{MD}(f_r,u) = \left(\int_{-\frac{T_m}{2}}^{\frac{T_m}{2}} x(t,u)\,e^{-j2\pi f_r t}dt\right)e^{j\emptyset_{MD}(u)} \qquad (17)$$

where $x(t,u) = \left(\int_a^b \tilde{s}(f_r,u)\,e^{j2\pi f_r t}df_r\right)e^{\left(j\frac{\emptyset_{MD}(u)\gamma}{f_c}t\right)}$, a and b are minimum and maximum range frequencies, respectively.

These steps are repeated several times to increase the accuracy of the estimation. However, in the case of the low SNR or contrast the performance of the algorithm may reduce. To overcome this issue, as reported in [17], the local images expressed by (13) and (14) are formed on a logarithmic scale, the dynamic range narrowed, and local centering performed.

$\tilde{s}_{MD}(f_r,u)$ still includes some range walk and higher order phase errors. Hence, PGA is implemented to correct the residual space-invariant errors. As described in [18], PGA has four main steps which are circular shifting, windowing, phase gradient estimation and iterative phase correction. However, in stripmap mode, the data must be divided into N_b azimuth blocks to avoid aliasing [19]. For PGA, the sub-aperture time, u_s, can be specified by (18). Here, u_s must be given the maximum value it can get to improve space-invariant phase error estimation.

$$u_s \leq \frac{R_0 \lambda f_{PRF}}{2v^2} \tag{18}$$

where λ is the wavelength.

After determining the sub-aperture time, the signal is de-chirped in a similar way shown in (12). Also, the window matrix, w_e, is used in this process following that described in (12). Subsequently, conventional PGA steps are implemented as described in [18] for each sub-aperture. In this way, the phase error function of each sub-aperture is obtained. Then, the error function, $\emptyset_i(u)$, is generated for each sub-aperture. In this function, the outside of the relevant sub-aperture time is set to zero. By using overlapped apertures, the phase information among sub-apertures is obtained as in [20]. After extracting the linear phase difference between apertures, estimated phase errors are combined with each other based on their azimuth positions. For example, in the case of half-overlapped sub-apertures, $\emptyset_{PGA}(u)$ is obtained as

$$\emptyset_{PGA}(u) = \begin{cases} \emptyset_1(u), & \frac{-u_a}{2} \leq u < \frac{2u_s - u_a}{2} \\ \emptyset_i(u) + \alpha_i, & \frac{2(i-1)\,u_s - u_a}{2} \leq u < \frac{(i+1)u_s - u_a}{2} \end{cases} \tag{19}$$

where i is ith $(\mathrm{i} = 2,\cdots,N_b)$ sub-aperture and α_i is the extracted linear phase difference between ith and $(i-1)th$ sub-aperture.

The phase error function is applied to data in the same way as described by (17). The phase error corrected data is given by the following equation.

$$\tilde{s}_{PGA}(f_r,u) = \left(\int_{-\frac{T_m}{2}}^{\frac{T_m}{2}} \tilde{x}(t,u) e^{-j2\pi f_r t} dt \right) e^{j\emptyset_{PGA}(u)} \tag{20}$$

where $\tilde{x}(t,u) = \left(\int_a^b \tilde{s}_{MD}(f_r,u)\, e^{j2\pi f_r t} df_r \right) e^{\left(j\frac{\emptyset_{PGA}(u)\gamma}{f_c} t\right)}$.

C. Azimuth & Range Blocks Based Phase Error Estimation

After PGA autofocus, RCMC is done as described in [2]. At this point, the generated image suffers from space-variant phase errors which are examined in Section II. Therefore, the image is divided into the azimuth and range blocks, and N_{LS} local scenes are created. By implementing PGA to each local scene, the residual phase error, $\emptyset_{LS_g}(u)$, is estimated, and compensated within each local scene as

$$\tilde{s}_{LS_g}(f_r,u) = \tilde{s}_{PGA}(f_r,u) e^{j\emptyset_{LS_g}(u)} \tag{21}$$

where $\tilde{s}_{LS_g}$ is gth $(\mathrm{g} = 1,2,\cdots,N_{LS})$ phase error corrected local scene.

At this point, the data can be expressed as

$$\tilde{s}_{LS} = \left[\tilde{s}_{LS_1},\ \tilde{s}_{LS_2},\cdots,\tilde{s}_{LS_{N_{LS}}}\right] \tag{22}$$

Then, a further LQMD is applied to each range block, based on azimuth block sizes, to suppress phase discontinuities between azimuth blocks. In this way, the data, $\tilde{s}_{LSMD}(f_r,u)$, is obtained. The Fourier transform of this data, $\tilde{S}_{LSMD}(f_r,f_a)$, is multiplied by the Fourier transform of the reference function, $H(f_r,f_a)$. By taking the inverse Fourier transform of this multiplication, the focused image is produced as

$$\tilde{s}_F(f_r,u) = \int_{\frac{-f_{PRF}}{2}}^{\frac{f_{PRF}}{2}} \tilde{S}_{LSMD}(f_r,f_a) \cdot H(f_r,f_a) e^{-j2\pi f_a u}\, df_a \tag{23}$$

where $H(f_r,f_a) = \int_{\frac{-u_a}{2}}^{\frac{u_a}{2}} e^{j\pi\frac{2v^2u^2}{\lambda r}} \cdot e^{-j2\pi f_a u}\, du$.

IV. Simulation

Using 36 point targets, a simulation has been implemented to examine the performance of the algorithm. The parameters used in the simulation are given in Table I. The heights of the four targets are adjusted to be 5 m and the others are set at 0 m. The GPS/INS data from the real-world trial is used to generate the trajectory deviations shown in Fig. 5 (a).

TABLE I. SIMULATION PARAMETERS

Operating Frequency	77 GHz
Bandwidth	1 GHz
Azimuth Beamwidth	14°
The Scene Size	$40\,m \times 36\,m$
Velocity	5 m/s
Altitude	20 m
Number of targets	36
PRF	2 kHz
Sweep Time	20 µs

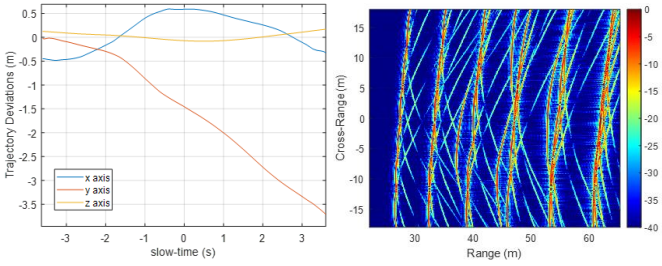

(a) (b)

Fig. 5. (a) The given motion error. (b) Range compressed data.

In Fig. 5 (b), the range compressed data is shown. At first, GPS/INS based MoCo is implemented as described in the previous section. The assumed GPS/INS error in the simulation is demonstrated in Fig. 6 (a). The calculated phase error using equation (4) is shown in Fig 6 (b). After range walk error correction and phase error compensation, the prominent targets must be selected from within the coarse image. Here, although all the targets have the same quality, only the four targets which have a 5 m height are chosen to show the impact of the targets'

height on the autofocus process. A coarse image is generated with a 20 cm azimuth resolution as shown in Fig. 6 (c). Selected targets are shown in the yellow rectangles. Using the location of the selected targets and the footprint of the beam, the window matrix, w_e, is created as described in the previous section. The range compressed data becomes as illustrated in Fig. 6 (d) after the windowing operation.

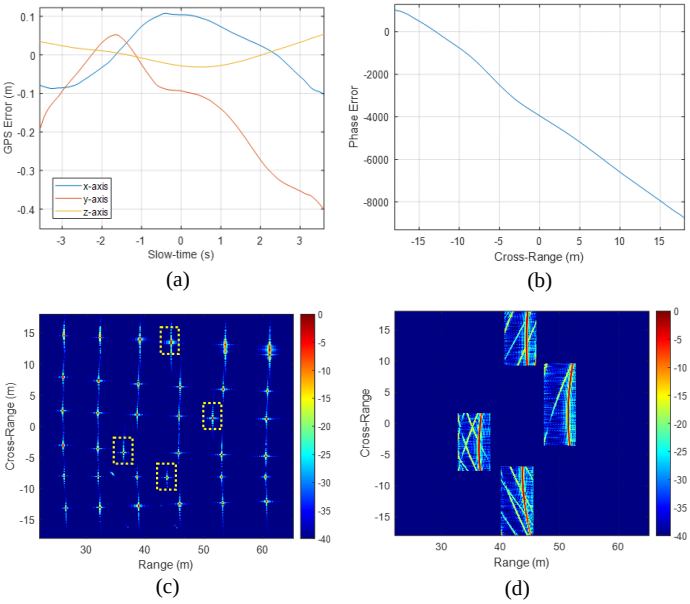

Fig. 6. (a) GPS/INS error. (b) The phase error calculated using GPS/INS data. (c) The coarse image after GPS/INS based MoCo. (d) The data after multiplication with the window matrix, w_e.

The space-invariant phase error estimation is made using this data set. For the LQMD autofocus, the data is divided into 18 half-overlapped azimuth blocks. Then, the steps described in Section III are repeated. The estimated result is subsequently shown in Fig. 7 (a). Using (17), range-walk is corrected, and the phase error is compensated based on the estimation result.

The residual space-invariant phase error is estimated by PGA and as illustrated in Fig. 7 (b). In the PGA step, the data is not divided into azimuth blocks because the PRF is chosen to be high enough to avoid aliasing. After compensating the residual range-walk and phase errors, the RCMC step is completed. At this point, the obtained image is shown in Fig. 8. After RCMC, the scene is divided into three azimuth and three range blocks as shown in Fig. 7 (c). As seen, nine local scenes are created. At first, PGA is applied to each local scene. Then, by implementing LQMD to each range block, the phase corrected data is obtained without discontinuities in the cross-range direction. The estimated phase errors from 9 local scenes by PGA are shown in Fig. 7 (d) after removing discontinuities in the cross-range direction by LQMD.

The result obtained after azimuth compression is shown in Fig. 9. This result is compared with the image obtained after the RCMC step (Fig. 8). Most of the targets in the image shown in Fig. 8 is not focused especially well. However, after azimuth/range-block based phase error compensation, most of the remaining residual errors are eliminated, and a 2 cm resolution is achieved (Fig. 9). As an example, one of the target's cross-range profiles is shown at different processing

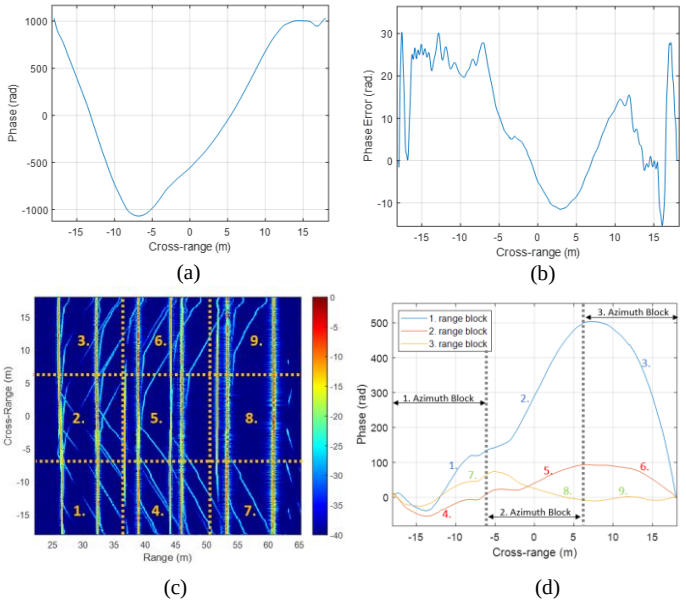

Fig. 7. (a) LQMD phase error estimation. (b) PGA phase error estimation. (c) The azimuth/range blocks. (d) Estimated phase errors in each block.

stages in Fig. 10. Also, when the three targets in the red rectangle are examined, it is seen that whereas the target at the mid-point is focused, the others are unfocused in Fig. 8 (d). The main reason for this is the height difference amongst the targets. The first and the third targets have a height of 0 m and the second target has a height of 5 m. The phase error was estimated using the second target, so no focusing problem is observed related to this target. However, the others do have significant phase errors. After phase compensation within the local scenes, some focusing problems still exist in the area shown by the red rectangle in Fig. 9 due to the height difference between targets. However, here, the second target is unfocused whereas others are focused. This is because the number of targets having 0 m height is more in the local scenes, so they contribute more to

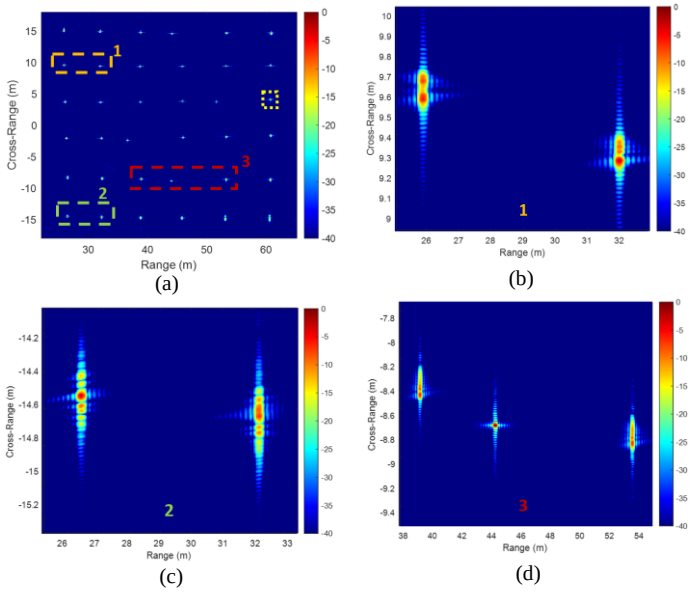

Fig. 8. (a) The obtained image after RCMC step. (b) The first local scene shown in orange rectangle in (a). (c) The second local scene shown in green rectangle in (a). (d) The third local scene shown in red rectangle in (a).

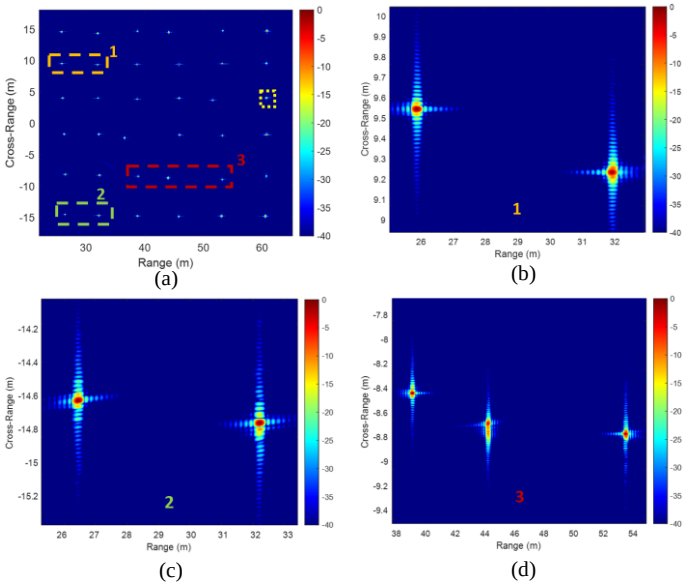

Fig. 9. (a) The final image. (b) The first local scene shown in orange rectangle in (a). (c) The second local scene shown in green rectangle in (a). (d) The third local scene shown in red rectangle in (a).

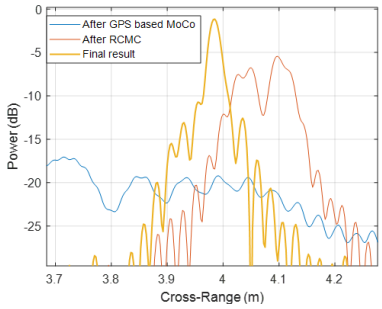

Fig. 10. Cross-range profile of the target in the yellow rectangle in Fig. 8.

the phase error estimation. The only way to correctly focus all three targets at the same time is to create separate local scenes for each target. Nevertheless, reducing the range block size is not always useful for real-world implementation. As a result, the target's height plays an important role in phase error estimation and compensation. Even low target height differences cause focusing problems. Therefore, compensating phase errors globally is highly difficult without knowing or estimating targets' heights. Our aim here is to produce correctly focused SAR images by compensating phase errors as much as possible within local scenes which have less target height variation without considering height-dependent errors.

V. Experimental Setup and Results

A SAR system was formed by using a 77 GHz INRAS radar mounted on a DJI S900 drone together with an A3 flight controller and a Raspberry-Pi microcontroller. The overall cost of the system is roughly £15K. The radar is controlled by a laptop remotely via the Raspberry-Pi. The Pi also stores the radar raw data and the GPS/IMU data. The max data transfer speed between the radar and the Raspberry-Pi is approximately 300 Mbps. The IMU refresh rate is 40 Hz and the GPS update rate is 10 Hz. The resulting positional accuracy is between 0.5 m and 1 m. The drone-borne SAR system is shown in Fig. 11 and explained in detail in [21]. The radar parameters of the

Fig. 11. Drone-borne SAR system.

system are given in Table II. The scene size is 67 m in azimuth and 43 m in the down-range direction.

Experiments were carried out at Deenethorpe Airfield in the United Kingdom setting the bandwidth of the radar to 1 GHz, giving a nominal range resolution of 15 cm. The experimentation site is shown in Fig. 12 (a). The photo was taken from a camera on the drone during flight. The drone was flown at an altitude of 20 m at a speed of 5 m/s.

TABLE II. RADAR PARAMETERS

Operating Frequency	77 GHz
Bandwidth	1 GHz
Azimuth Beamwidth	13.2°
Elevation Beamwidth	51°
Tx/Rx Antenna gains	16 dBi
Transmit Power	10 dBm
Sweep Time	204.8 µs
Used Transmit and Receive Channels	1-Tx, 1-Rx
Noise Figure	~12 dB
System Losses	~ 3 dB
Weight	0.41 kg
Look Angle	60°

The image before any MoCo is displayed in Fig. 12 (b). As can be observed, the signal-to-noise ratio (SNR) is rather low, and the image is poorly focused. The smoothed GPS record is shown in Fig. 13 (a). Only the GPS record is used because using IMU/INS data does not improve the result significantly. The calculated phase error using equation (4) is illustrated in Fig. 13 (b) where the linear phase error has been compensated. After the GPS based MoCo and Doppler centroid steps (shown in Figs. 3 and 4) the range compressed data shown in Fig. 14 (a) is obtained. Further, a Kaiser weighting is applied in the range dimension to reduce sidelobes. The resulting image can be seen in Fig. 12 (c). In this image, 14 prominent targets shown in orange circles are selected. According to the location of the selected targets and the beam footprint size, the window matrix, w_e is created as described in Section III. This differently range compressed data is shown in Fig. 14 (b) after multiplication by w_e. In this figure, the selected targets' range histories can be seen. The space-invariant phase error estimation is done using this data. In the LQMD step, 60 half-overlapped azimuth blocks are created, and steps described in Section III are implemented. The range walk and phase errors are corrected using equation (17). After four iterations, the phase error is estimated as that shown in Fig. 15 (a).

After LQMD, PGA is implemented to compensate residual higher order errors. The PRF is chosen to be 2 kHz. As seen from equation (18), PGA cannot be implemented directly. By considering the windowed data, three half-overlapped sub-apertures are created so that aliasing is avoided. After de-

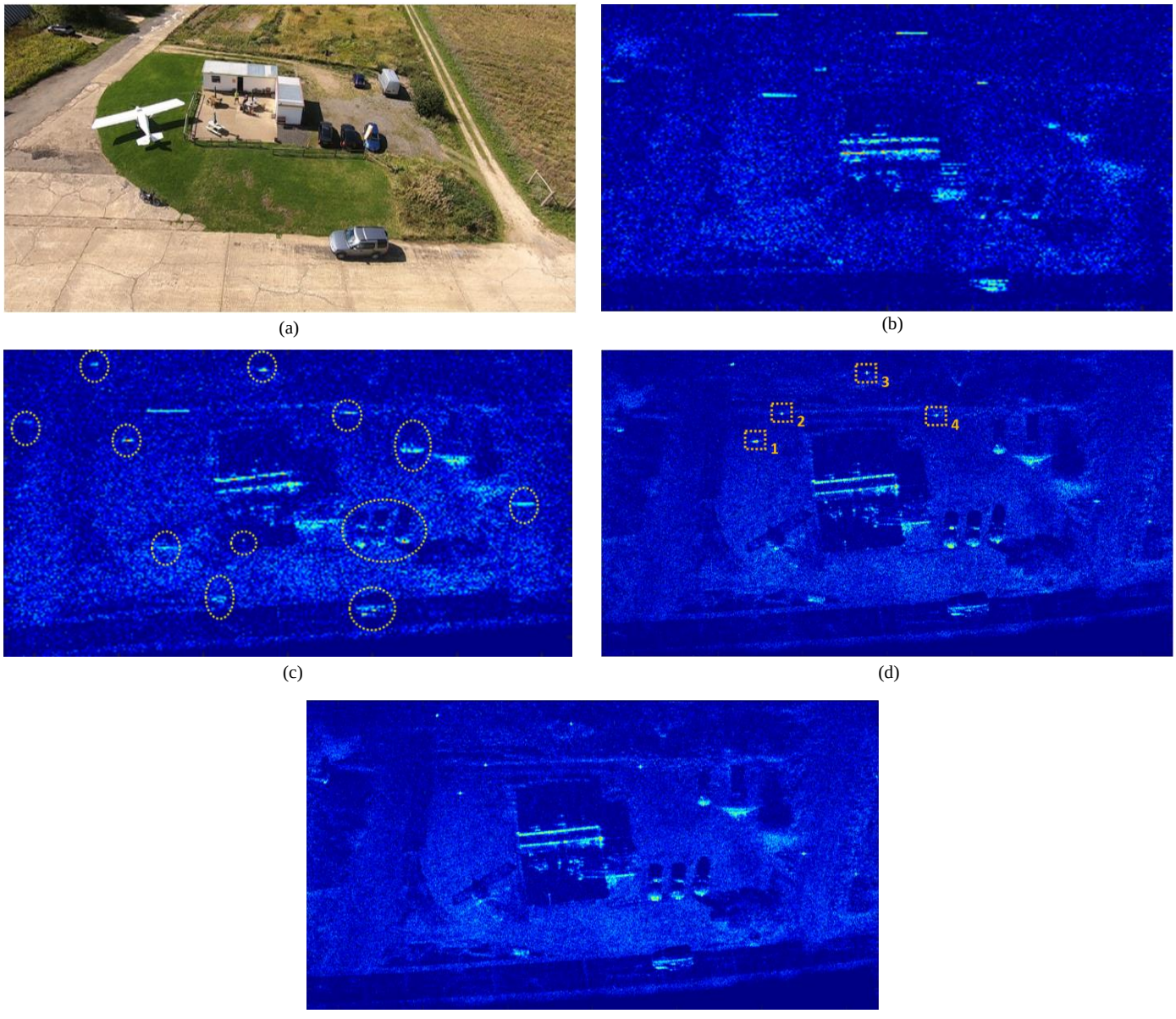

(a) (b) (c) (d) (e)

Fig. 12. (a) A picture from the experimentation site. (b) The image without MoCo. (c) The image with MoCo using GPS data. (d) The image after the RCMC step. (e) The final image after azimuth and range blocks based MoCo.

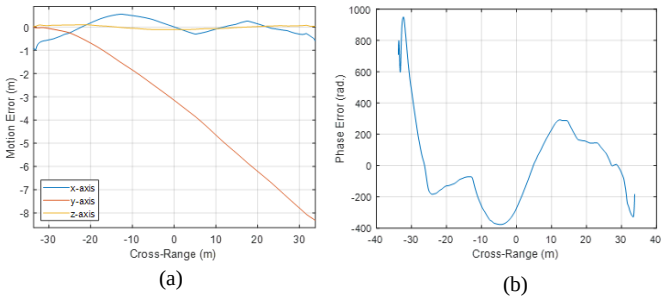

(a) (b)

Fig. 13. (a) GPS measured deviation from the ideal sensor track. (b)The phase error according to GPS without the linear term.

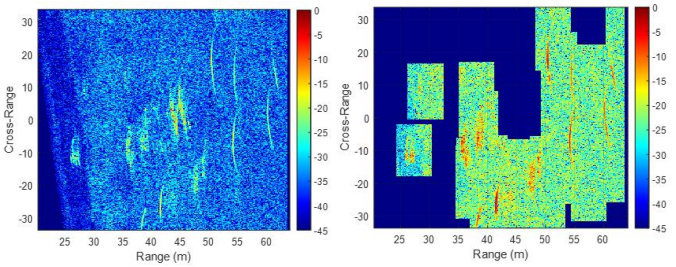

(a) (b)

Fig. 14. (a) The range compressed data after GPS based MoCo. (b) The data after multiplication with the window matrix, w_e.

chirping the data, PGA steps are applied as per Section III. The estimation result is shown in Fig. 15 (b). Again, the range-walk and phase errors are corrected as in (20). As can be seen, LQMD estimates high magnitude but low frequency phase errors, whereas PGA estimates low magnitude but high frequency phase errors. In this way LQMD and PGA complement each other well. Fig. 12 (d) shows the formed image after space-invariant error compensation and the RCMC step. Here, the image structures and individual objects start to become much better defined, along with shadows that they cast. However, this

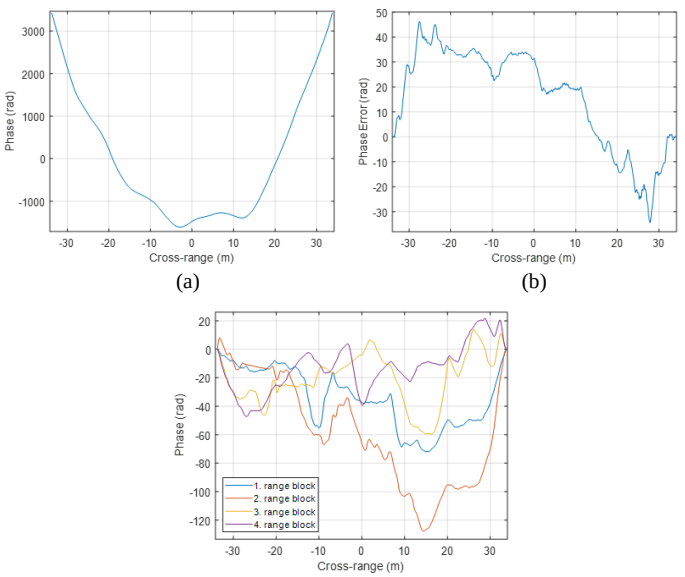

Fig. 15. (a) LQMD phase error estimation. (b) PGA phase error estimation. (c) Estimated phase errors in each azimuth and range blocks by PGA after reducing discontinuities in the cross-range direction by LQMD.

image is still not in perfect focus at all pixels. In order to compensate remaining phase errors, the image is divided into 5 azimuth and 4 range blocks. As a result, 20 local scenes are generated, and PGA is implemented on each one. Following this step, LQMD is implemented to each range block to decrease discontinuities between azimuth blocks. Here, local images are translated onto a logarithmic scale and hence the dynamic range is narrowed to improve the phase error estimation (as explained in Section III). After reducing discontinuities in the cross-range direction by LQMD, the estimated phase error from each local scene by PGA is illustrated in Fig. 15 (c). After phase error compensation, the image shown in Fig. 12 (e) is formed by azimuth compression. Resolutions of 1.7 cm cross-range and 16 cm down-range are obtained verified through measurement of the response from point targets. When Fig. 12 (d) and Fig. 12 (e) are compared with each other, it seems that there is no significant difference between them, at first glance. However, if the corner reflector shown in the 1st rectangle in Fig. 12 (d) is compared with that of Fig. 12 (e) the difference can be seen clearly. This comparison is demonstrated in both Fig. 16 and Fig. 17 (a). In addition, the cross-range profiles of the other two corner reflectors in the 2nd and 3rd rectangles are shown in Fig. 17 (b) and 17 (c), respectively. As seen, azimuth and range blocking

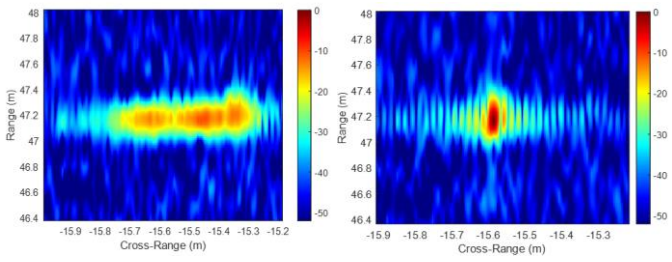

Fig. 16. (a) The corner reflector shown in the 1st rectangle in Fig. 12 (d). (b) The same corner reflector in the final image (Fig. 12 (e)).

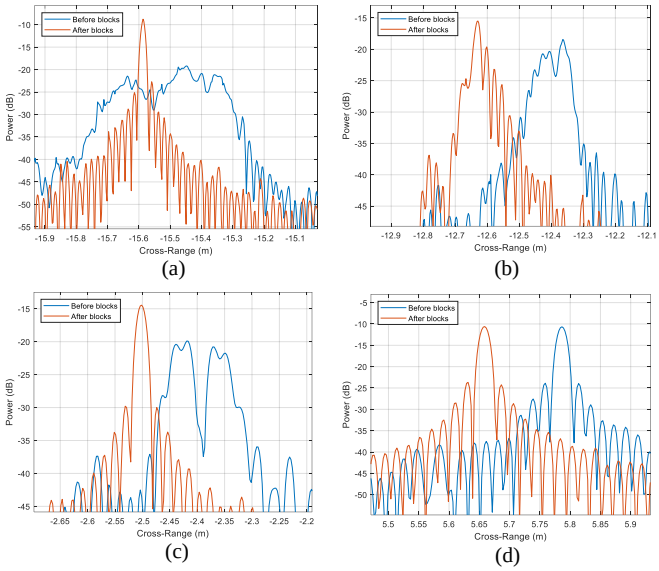

Fig. 17. Comparison of the corner reflectors in the dashed rectangles shown in Fig. 12 (d) with Fig 12 (e). (a). The 1st reflector. (b) The 2nd reflector. (c) The 3rd reflector. d) The 4th reflector.

based autofocus improves the overall image quality. The other corner reflector in the 4th rectangle is well focused in both images (Fig. 17 (d)). There is only a linear shift between them.

In Fig. 12, it can be seen that there is a very good correspondence between the optical image and the SAR images. The cars, motorbike, roads and cracks on the roads can be easily observed in the SAR image. Due to low reflections from the aircraft, it is a little indistinct, but the radar shadow of the aircraft is obvious.

VI. Conclusion

In this paper, we have shown, for the first time, that a cross-range resolution of less than 2 cm can be achieved using a low-cost high-frequency vehicular radar mounted onboard a low-cost commercially available drone at short but highly useful ranges. After evaluating the motion errors and discussing possible difficulties in the image formation, an algorithm suitable for production of high-resolution imaging at 77 GHz has been developed. The performance of the algorithm has been validated through both simulation and experiment. Although this particular MoCo strategy does not compensate the phase errors perfectly over all of the imaged area, the results show practical usability at short ranges for which many applications may be envisaged. It is also noting that this is an example result from multiple experiments conducted at different locations. In each case similar results have been obtained. On the other hand, wrong strong target selection and high target height variation in the scene can degrade the performance of the algorithm. The next goal will be making the selection of strong targets automatic and to include height-dependent target focusing using digital elevation models to aid imaging quality and robustness.

REFERENCES

[1] M. Soumekh, Synthetic aperture radar signal processing : with MATLAB algorithms / Mehrdad Soumekh. New York ; Chichester: Wiley, 1999.

[2] Cumming I.G., Wong F.H. (2005), Digital processing of Synthetic Aperture Radar data, Artech House.

[3] M. García Fernández *et al*., "Synthetic Aperture Radar Imaging System for Landmine Detection Using a Ground Penetrating Radar on Board a Unmanned Aerial Vehicle," in *IEEE Access*, vol. 6, pp. 45100-45112, 2018, doi: 10.1109/ACCESS.2018.2863572.

[4] M. Garcia-Fernandez, Y. Alvarez-Lopez, B. Gonzalez-Valdes, Y. Rodriguez-Vaqueiro, A. Arboleya-Arboleya and F. L. Heras, "Recent advances in high-resolution Ground Penetrating Radar on board an Unmanned Aerial Vehicle," 2019 13th European Conference on Antennas and Propagation (EuCAP), Krakow, Poland, 2019, pp. 1-5.

[5] E. Schreiber, A. Heinzel, M. Peichl, M. Engel and W. Wiesbeck, "Advanced Buried Object Detection by Multichannel, UAV/Drone Carried Synthetic Aperture Radar," 2019 13th European Conference on Antennas and Propagation (EuCAP), Krakow, Poland, 2019, pp. 1-5.

[6] M. Schartel, R. Bähnemann, R. Burr, W. Mayer and C. Waldschmidt, "Position Acquisition for a Multicopter-Based Synthetic Aperture Radar," 2019 20th International Radar Symposium (IRS), Ulm, Germany, 2019, pp. 1-7, doi: 10.23919/IRS.2019.8768172.

[7] Y. A. Su, W. Liu, H. Feng and B. P. Ng, "Study of multi-rotor UAV SAR processing," 2017 IEEE Radar Conference (RadarConf), Seattle, WA, 2017, pp. 0226-0232, doi: 10.1109/RADAR.2017.7944202.

[8] M. Ding, C. Ding, L. Tang, X. Wang, J. Qu and R. Wu, "A W-Band 3-D Integrated Mini-SAR System With High Imaging Resolution on UAV Platform," in IEEE Access, vol. 8, pp. 113601-113609, 2020, doi: 10.1109/ACCESS.2020.3003273.

[9] M. Lort, A. Aguasca, C. López-Martínez and T. M. Marín, "Initial Evaluation of SAR Capabilities in UAV Multicopter Platforms," in IEEE Journal of Selected Topics in Applied Earth Observations and Remote Sensing, vol. 11, no. 1, pp. 127-140, Jan. 2018, doi: 10.1109/JSTARS.2017.2752418.

[10] Hu, Xianyang et al. "Imaging for Small UAV-Borne FMCW SAR." Sensors (Basel, Switzerland) vol. 19,1 87. 27 Dec. 2018, doi:10.3390/s19010087.

[11] S. Zhou, L. Yang, L. Zhao and G. Bi, "Quasi-Polar-Based FFBP Algorithm for Miniature UAV SAR Imaging Without Navigational Data," in IEEE Transactions on Geoscience and Remote Sensing, vol. 55, no. 12, pp. 7053-7065, Dec. 2017, doi: 10.1109/TGRS.2017.2739133.

[12] X. Mao, D. Li, L. Ding, and D. Zhu, "Signal processing for multi-rotors UAV SAR," in Proceedings of IET International Radar Conference, Nanjing, China, Oct. 2018.

[13] Z. Xu and D. Zhu, "High-resolution miniature UAV SAR imaging based on GPU Architecture," J. Phys. Conf. Ser., vol. 1074, no. 1, p. 012122, Sep. 2018.

[14] O. O. Bezvesilniy, I. M. Gorovyi and D. M. Vavriv, "Estimation of phase errors in SAR data by Local-Quadratic map-drift autofocus," 2012 13th International Radar Symposium, Warsaw, 2012, pp. 376-381, doi: 10.1109/IRS.2012.6233350.

[15] Bezvesilniy, O., Gorovyi, I., & Vavriv, D. (2016). Autofocusing SAR images via local estimates of flight trajectory. *International Journal of Microwave and Wireless Technologies*, *8*(6), 881-889. doi:10.1017/S1759078716000180.

[16] Moreira, A., Mittermayer, J., and Scheiber, R.: 'Extended chirp scaling algorithm for air- and spaceborne SAR data processing in stripmap and ScanSAR imaging modes', IEEE Trans. Geosci. Remote Sens., 1996, 34, (5), pp. 1123–1136, doi: 10.1109/36.536528

[17] I. M. Gorovyi, O. O. Bezvesilniy and D. M. Vavriv, "A novel trajectory restoration algorithm for high-resolution SAR imaging," 2014 15th International Radar Symposium (IRS), Gdansk, 2014, pp. 1-4, doi: 10.1109/IRS.2014.6869242.

[18] D. E. Wahl, P. H. Eichel, D. C. Ghiglia and C. V. Jakowatz, "Phase gradient autofocus - a robust tool for high resolution SAR phase correction," in IEEE Transactions on Aerospace and Electronic Systems, vol. 30, no. 3, pp. 827-835, July 1994, doi: 10.1109/7.303752.

[19] D. G. Thompson, J. S. Bates, D. V. Arnold and D. G. Long, "Extending the phase gradient autofocus algorithm for low-altitude stripmap mode SAR," IEEE 1999 International Geoscience and Remote Sensing Symposium. IGARSS'99 (Cat. No.99CH36293), Hamburg, Germany, 1999, pp. 564-566 vol.1, doi: 10.1109/IGARSS.1999.773566.

[20] L. Zhang, J. Sheng, M. Xing, Z. Qiao, T. Xiong and Z. Bao, "Wavenumber-Domain Autofocusing for Highly Squinted UAV SAR Imagery," in *IEEE Sensors Journal*, vol. 12, no. 5, pp. 1574-1588, May 2012, doi: 10.1109/JSEN.2011.2175216.

[21] Ali Bekar, Michail Antoniou, Christopher J. Baker, "High-Resolution Drone-Borne SAR Using Off-the-Shelf High-Frequency Radars", submitted to 2021 IEEE Radar Conference, Atlanta, May 2021.